Light-Driven Hydrogen Evolution Reaction Catalyzed by a Molybdenum-Copper Artificial Hydrogenase

Raphaël J Labidi, Bruno Faivre, Philippe Carpentier, Giulia Veronesi, Albert Solé- Daura, Ragnar Bjornsson, Christophe Léger, Philipp Gotico, Yun Li, Mohamed Atta, et al.

Light-Driven Hydrogen Evolution Reaction Catalyzed by a Molybdenum-Copper Artificial Hydrogenase.

Raphaël J. Labidi[1], Bruno Faivre[1], Philippe Carpentier[2], Giulia Veronesi[2], Albert Solé-Daura[1], Ragnar Bjornsson[2], Christophe Léger[3], Philipp Gotico[4], Yun Li[1], Mohamed Atta[1,2] and Marc Fontecave[1*].

[1]Laboratoire de Chimie des Processus Biologiques, UMR 8229, Collège de France/CNRS/Sorbonne Université, 11, place Marcellin-Berthelot, Paris, France.

[2]Univ Grenoble Alpes, CNRS, CEA, IRIG, Laboratoire de Chimie et Biologie des Métaux, 17 rue des Martyrs, 38000 Grenoble, France.

[3]Laboratoire de Bioénergétique et Ingénierie des Protéines, CNRS, Aix Marseille Université, Marseille 13009, France.

[4]Laboratoire des Mécanismes Fondamentaux de la Bioénergétique, DRF/JOLIOT/SB2SM, UMR 9198 CEA/CNRS/I2BC, Gif Sur Yvette 91191, France

*To whom correspondence should be addressed.

Email: marc.fontecave@college-de-france.fr;

Keywords: hydrogenase, artificial enzyme, orange protein, molybdenum-copper clusters.

Abstract.

Orange Protein (Orp) is a small bacterial metalloprotein of unknown function that harbors a unique molybdenum/copper (Mo/Cu) heterometallic cluster, $[S_2MoS_2CuS_2MoS_2]^{3-}$. In this paper, the performance of Orp as a catalyst for the photocatalytic reduction of protons into H_2 has been investigated under visible light irradiation. We report the complete biochemical and spectroscopic characterization of *holo*-Orp containing the $[S_2MoS_2CuS_2MoS_2]^{3-}$ cluster, with docking and molecular dynamics simulations suggesting a positively charged Arg, Lys-containing pocket as the binding site. *Holo*-Orp exhibits an excellent photocatalytic activity, in the presence of ascorbate as the sacrificial electron donor and $[Ru(bpy)_3]Cl_2$ as the photosensitizer, for hydrogen evolution with a maximum turnover number of 890 after 4 hours irradiation. DFT calculations were used to propose a consistent reaction mechanism in which the terminal sulfur atoms are playing a key role in promoting H_2 formation. A series of dinuclear $[S_2MS_2M'S_2MS_2]^{(4n)-}$ clusters, with M = Mo^{VI}, W^{VI} and M'$^{(n+)}$ = Cu^{I}, Fe^{I}, Ni^{I}, Co^{I}, Zn^{II}, Cd^{II} were assembled in Orp, leading to different M/M'-Orp versions which are shown to display catalytic activity, with the Mo/Fe-Orp catalyst giving a remarkable TON of 1150 after 2.5 hours reaction and an initial turnover frequency (TOF°) of 800 h^{-1} establishing a record among previously reported artificial hydrogenases.

INTRODUCTION

Electro- and photo-reduction of water into H_2 or of CO_2 into energy-dense organic chemicals of economic value are key strategies for storing renewable and intermittent energies, such as solar energy into chemical energy (the energy in chemical bonds). The development of this technology obviously requires the discovery of cheap, stable, efficient and selective catalysts and better fundamental understanding of multi-electronic and multi-protonic mechanisms associated with the reaction at work. Besides largely developed solid and molecular catalysts, the enzymatic approach has mainly been explored for proton reduction to H_2 through in-depth studies of hydrogenases (H_2ases) and their biotechnological applications.[1-3] In contrast, enzymes selectively converting CO_2 into CO and formic acid, here named CO_2 reductases (CO_2Rases), such as carbon monoxide dehydrogenases (CODH) and formate dehydrogenases (FDH), respectively, using unique active sites based on non-noble metals, exist in nature but have been much less explored.[3-4] This is mainly due to the fact that these enzymes are very difficult to prepare in pure form as their production depends on complex maturation machineries and may be extremely sensitive to oxygen.[5] However, there have been successful attempts to couple them to electrodes or semiconductors.[6-12] Artificial enzymology comes up as a powerful alternative, as it provides the opportunity to combine attractive features of both molecular and enzymatic catalysis and expand the repertoire of enzymes. This is achieved by anchoring a synthetic molecular catalyst, such as an organometallic complex or an inorganic cluster, into a protein host, not necessarily an enzyme, through covalent or non-covalent interactions.[13] It is expected that, within an appropriate protein environment, the catalytic species might benefit from greater water solubility, activity, selectivity and stability. While the artificial enzymology strategy has begun to be explored for proton reduction catalysis, opening the way to artificial hydrogenases, ArH_2ases,[13-17] there are only few such hybrid systems for CO_2 reduction reported in the literature.[18-22]

Intrigued by the remarkable structural resemblance of the Mo-S-Cu cluster bound to the orange protein (Orp), a small monomeric protein of low molecular mass (~12 kDa, ~120 residues), and the heterodinuclear Mo/Cu active site in CODH (scheme 1), we have started a program aiming at studying the catalytic potential of the *holo*-Orp protein.[23] As shown by crystallographic structures, one class of bacterial CODH uses a unique Mo-S-Cu center in which the Mo ion enjoys a sulfur-rich coordination with one bidentate dithiolene ligand, namely molybdopterin, one oxo and one hydroxo ligand and is linked, via a sulfide bridge, to a Cu ion (scheme 1).[24] The Cu itself is coordinated by a cysteine ligand from the polypeptide

chain.[24] On the other hand, the inorganic species bound to the Orp, isolated from extracts of sulfate-reducing organisms, *Desulfovibrio gigas (Dg)*, by the group of José J. G. Moura, and of as yet unknown function, has been defined as an EPR-silent linear mixed-metal sulfide $[S_2MoS_2CuS_2MoS_2]^{3-}$ cluster (scheme 1).[23] The central Cu ion, in the Cu(I) state, is linked to two terminal Mo(VI) ions by sulfide bridges, as shown by metal quantitation, X-ray absorption fine structure (XAFS) spectroscopy[25] and comparison with a synthetic model compound.[26] While only the three-dimensional structure of the *apo*-protein is available,[27] NMR data obtained on the *holo*-OrpDg suggests that the cluster is stabilized inside the protein, in a rather well-identified position, by a combination of electrostatic and hydrophobic interactions, excluding covalent binding to protein residues.[28] Yet, the structure of the cluster-binding pocket remains elusive. Finally, J. J. G. Moura and collaborators nicely established that the cluster could be appropriately assembled into *apo*-Orp simply by reaction with tetra-thiomolybdate and a copper salt, using the appropriate stoichiometry.[29] Furthermore a $[S_2MoS_2M'S_2MoS_2]^{3-}$ cluster, with M'= Fe, Co, Ni,[30] as well as a $[S_2WS_2CuS_2WS_2]^{3-}$ cluster, in which W was substituted for Mo, can be assembled as well.[28] In the following, the different metalloprotein versions will be named M/M'-Orp in order to indicate which metals are present in the protein, M for the terminal atoms and M' for the central atom of the linear tri-metallic cluster.

While we investigated its catalytic properties and did not find any CO_2 photoreduction activity in water, we discovered that *holo*-Orp with a $[S_2MoS_2CuS_2MoS_2]^{3-}$ cluster is an efficient catalyst for proton reduction. Here, we report the characterization of a series of M/M'-Orp preparations and their evaluation as artificial hydrogenases using optimized visible light-driven proton reduction assays as well as DFT calculations aiming at giving atomic-level insight into the reaction mechanism of this unique catalytic cluster.

Results.

Preparation and characterization of the *holo*-OrpDg form containing a $[S_2MoS_2CuS_2MoS_2]^{3-}$ cluster. The *apo*-OrpDg (from *Desulfovibrio gigas*) and *apo*-OrpTm (from *Thermotoga maritima*) were purified as described in the supplementary information section. After the final step of purification, the purity was evaluated by SDS/PAGE to be >95% (SI, Figure S1). As shown by analytical gel filtration chromatography the protein is a stable monomer in solution as reported previously (SI, Figure S2).[23] The Mo/Cu-OrpDg, containing a $[S_2MoS_2CuS_2MoS_2]^{3-}$ cluster, was prepared as described previously by reconstitution of the *apo*-form with a mixture of $CuCl_2$ and tetrathiomolybdate (TTM,

$[NH_4]_2MoS_4$) salt.[28] After desalting, metal analysis of Mo/Cu-OrpDg showed the presence of ~ 2 Mo and 1 Cu atoms bound to a monomer.

The structural integrity of the $[S_2MoS_2CuS_2MoS_2]^{3-}$ cluster in Mo/Cu-OrpDg was substantiated by UV/Visible and XAFS spectroscopies. In Figure 1 is shown the light absorption spectrum of Mo/Cu-OrpDg, which displays absorption maxima at 340 and 480 nm and a shoulder at 430 nm characteristic of S→Mo charge-transfer bands.[25] The optical properties described here are in excellent agreement with those of both native and reconstituted Mo/Cu-OrpDg that had been previously described.[23, 30] The presence of a $[S_2MoS_2CuS_2MoS_2]^{3-}$ cluster into Mo/Cu-OrpDg was further supported by Cu K-edge XAFS spectroscopy (Figure 2). The features of the near-edge region (X-ray Absorption Near-Edge Structure, XANES) of the spectrum are similar to those reported for native Mo/Cu-OrpDg isolated from *D. gigas*.[25] A weak pre-edge peak at approximately at ~ 8982 eV is indicative of Cu(I) oxidation state[31-32] (Figure 2A). The extended region of the spectrum (Extended X-ray Absorption Fine Structure, EXAFS), Fourier-Transformed into the real space or as extracted in the reciprocal space, is shown in Figure 2B and 2C, respectively. The former (Figure 2B) displays two major features between 2 and 3 Å (black dashed curve), which were initially fitted with a simple two-components model to account for an atomic shell of S atoms and one of Mo atoms around the Cu absorber. The simulated Cu-S and Cu-Mo contributions are reported as green and blue curves, respectively, in Figure 2B, and the best fitting curve given by their sum as a red curve. The latter was obtained with a number of S neighbors of 3.5±0.3, slightly less than the expected number of 4, and a number of Mo atoms of 2.0±0.3. The distances and Debye Waller factors are in good agreement with previously reported values.[25] We observed a slight difference in the Cu-S distance, which is estimated as 2.32±0.02 Å , longer than the value of 2.21 Å reported for the as-isolated Mo/Cu-OrpDg protein,[25] but still in the expected range for a Cu-S bond length, while the Cu-Mo distance is fully consistent with that reported for the as-isolated Mo/Cu-OrpDg protein.[25] In order to corroborate the integrity of the $[S_2MoS_2CuS_2MoS_2]^{3-}$ cluster, we fitted the EXAFS spectrum directly in the reciprocal space, using the full cluster as a starting model for *ab initio* calculations. We included in the fit all the single scattering paths (Cu-S first neighbors, Cu-Mo, Cu-S2 with outer-shell S) and the 7 most intense multiple scattering paths. The theoretical signal (red curve) was fitted to the experimental EXAFS spectrum (black, dashed curve), providing a fair agreement (Figure 2C). The resulting best-fitting values are accurate and physically meaningful, as reported in Tables S1 and S2. They include interatomic distances (R) and Debye-Waller factors (σ^2) for the three atomic shells around the Cu

absorber, and a Debye-Waller factor common to all multiple scattering paths (σ^2_{MS}). All these data, reported for the first time for the reconstituted Mo/Cu-OrpDg, nicely demonstrate that the $[S_2MoS_2CuS_2MoS_2]^{3-}$ cluster is correctly assembled within the protein. Mo/Cu-OrpTm was prepared similarly, with the presence of a $[S_2MoS_2CuS_2MoS_2]^{3-}$ cluster, as shown by metal quantitation and UV-Visible spectroscopy (Figure S3A).

A structural model of Mo/Cu-OrpDg: $[S_2MoS_2CuS_2MoS_2]^{3-}$ cluster docking into *apo*-OrpDg. Since all our efforts to crystallize Mo/Cu-OrpDg and Mo/Cu-OrpTm proved unsuccessful so far, we conducted an "*in silico*" docking approach, using the program Molegro Virtual Docker (MVD), in order to predict the most probable binding modes of the $[S_2MoS_2CuS_2MoS_2]^{3-}$ cluster into *apo*-OrpDg. The docking calculations, described in the experimental section, were carried out using the crystal structure of *apo*-OrpDg (Figure 3A1 & A2) deposited in Protein Data Bank with entry 2WFB[27] and that of the compound $[PPh_4][Et_4N]_2[S_2MoS_2CuS_2MoS_2]$ (Figure 3B) deposited in Cambridge Crystallographic Data Centre with the entry RADWUP-224742.[26] For the sake of simplicity, we settled a symmetric structure for the cluster $[S_2MoS_2CuS_2MoS_2]^{3-}$ defined as the average of its resonant forms. Thus, the global charge is homogeneously distributed over the 4 terminal sulfur atoms so that each one bears an apparent charge of -3/4e and linked to Mo atoms by bonds of mixed hybrid breed (Figure 3-B). The MVD program first computed the electrostatic potential surface of the protein (Figure 3C1 and 3C2). It showed a unique well-delimited excavated area of the protein bearing a strikingly positive charge (in dark blue in Figures 3C1 & C2), well designed for interacting with the negatively charged metal-cluster. Consistently, positively charged residues, Arg-23, Arg-26, Lys-79 and Lys-120, border that pocket (Figure 3A2). The software was also able to identify an empty volume (~ 41 $Å^3$) at the surface of the protein (Figure 3D) having the appropriate size to accommodate the metal-cluster, furthermore exactly matching the positive area computed at the previous step. It is worth mentioning that, in the *apo*-OrpDg structure 2WFB, this pocket hosts a cluster of 3 phosphate anions (PO_4^-) arising from the crystallization buffer. Altogether, these data constitute a set of indicators strongly suggesting that this pocket is the binding site of the metal-cluster.[27] Then, a sequence of 10 independent runs of docking simulations was carried out using the MolDock algorithm.[33] The computational procedure and the associated parameters are described with more details in the supporting information document, "Molecular Docking" section. The structure of the best docking pose is shown in Figure 3E, 3F and 3G). It confirmed that the metal-cluster fits perfectly in the volume of the positively charged surface pocket. In this structure, Arg-23,

Arg-26, Lys-79 and Lys-120 side chains have slightly moved in the pocket allowing them to interact with the metal-cluster via hydrogen bonds and electrostatic interactions.

Molecular Dynamics Simulation Study. Molecular dynamics simulations (see experimental section for details) starting from the docked structure revealed that the $[S_2MoS_2CuS_2MoS_2]^{3-}$ complex was stable within the predicted binding pocket during the whole simulation time of 1 μs (Figure 4, top). Interestingly, placing the complex far away from this binding pocket and running a new simulation led to spontaneous displacement of the complex into the same pocket within 15 ns, where it remained for the rest of the 1 μs simulation (Figure 4, bottom).
Shown in Figure 4 are representative structures of that simulation highlighting the conformation of the complex within the binding pocket, surrounded by the cationic residues: Lys-79, Arg-23, Arg-26 and the neutral His-53. While the C-terminus Lys-120 residue is part of the binding pocket (containing 3 PO_4^- anions) in the *apo*-OrpDg X-ray structure,[27] the highly flexible[28] C-terminal peptide (residues 113-120) was absent from the binding pocket during most of the simulation. In a simulation without the complex, the Lys-120 residue was also predicted to be mostly absent from this pocket. Whether Lys-120 is involved in the binding of the $[S_2MoS_2CuS_2MoS_2]^{3-}$ complex is hence unclear at present.
While these classical simulations only give an approximate representation (see DFT section for electronic structure calculations) of the complexity of the inorganic electronic structure of the $[S_2MoS_2CuS_2MoS_2]^{3-}$ complex (described by a simplistic nonbonding model of atomic charges and Lennard-Jones parameters) as well as of the electrostatic interactions with the protein, they clearly suggest that a $[S_2MoS_2CuS_2MoS_2]^{3-}$ complex is likely to bind and remain in the identified positively charged binding pocket.

Photocatalytic hydrogen evolution catalyzed by Mo/Cu-OrpDg. The ability of *holo*-Orp to catalyze the reduction of protons into hydrogen was carried out in water under anaerobic conditions and visible light irradiation using a three-component homogeneous system, comprising the catalyst (*holo*-Orp), a photosensitizer ($[Ru(bpy)_3]Cl_2$), and a sacrificial electron donor (sodium L-ascorbate). An initial reaction was carried out by mixing 5 μM of Mo/Cu-OrpDg containing 0.1 mM of $[Ru(bpy)_3]^{2+}$ and 100 mM sodium L-ascorbate in 100 mM phosphate buffer, pH 6.8 and irradiated with visible light using a Xe lamp (as described in the experimental section).
H_2 evolution was monitored by analysis of the headspace with gas chromatography. As shown in Figure 5A (red circles), the system is functional and photocatalytic production of H_2

proceeds linearly for about 30 min, corresponding to an initial turnover frequency (TOF°) of about 127 h^{-1}. From then, the reaction rate slowly decreased, reaching a plateau after four hours reaction, yielding a turnover number (TON) of 266. In a control experiment, omitting Mo/Cu-OrpDg from the reaction mixture, much lower amounts of H_2 were produced, demonstrating the catalytic role of Mo/Cu-OrpDg (Figure 5A black circles, and Figure S5). In the absence of $[Ru(bpy)_3]^{2+}$ or sodium L-ascorbate, no H_2 was formed (Figures S4 & S6).

Photoreaction Conditions Optimization. An extensive series of experiments were carried out to optimize the system in terms of H_2 evolution catalytic activity. For that purpose, various reaction mixtures were studied using different concentrations of the catalyst (0 -15 µM), the photosensitizer (0 - 1500 µM), the electron donor sodium L-ascorbate (0 - 0.3 M) and different buffer pH (4.7 - 7.8). The data are shown in Figures S4-S7. They showed: (i) increased activity upon increasing photosensitizer concentrations up to 700 µM (Figure S4); (ii) increased activity upon increasing catalyst concentration (Figure S5); (iii) the need of sodium L-ascorbate for photocatalysis but with little effect between 50 - 300 mM concentration range (Figure S6). Finally, decreasing the pH, *i.e.* increasing the proton substrate concentration, had a large stimulatory effect on the activity, with citrate-based buffer giving higher activity than phosphate-buffer at the same pH (Figure S7). The largest TOF° (~ 700 h^{-1}) and TON_{4h} (~ 890) values were obtained in this study using 5 µM Mo/Cu-OrpDg, 0.7 mM $[Ru(bpy)_3]^{2+}$, 0.1 M sodium L-ascorbate in pH 5.2 citrate buffer (Figure 5B).

Figure S8 furthermore shows a clear trend in which it takes a longer time for the production of H_2 to start to level off as pH is increased: 20 min (pH 5.2), 30 min (pH 5.8); 50 min (pH 5.8), 150 min (pH 6.8); while no inactivation could be observed during 4 h at pH 7.8. This reflects a pH-sensitivity of the protein. Thus, at the most acidic conditions allowing the largest activity, the system suffers from a significant instability. As a further confirmation, at pH 5.2, once the catalytic plateau is reached, H_2 production only slightly resumed upon addition of a fresh solution of $[Ru(bpy)_3]^{2+}$ (by 18% with respect to the initial TOF of the first run, Figure S9A). However, other sources of inactivation at this pH have to be considered since addition of both Mo/Cu-OrpDg and $[Ru(bpy)_3]^{2+}$ after 2 h only led to a TOF value corresponding to 40% of the initial TOF of the first run (Figure S9B).

Another source of inactivation proved to be Orp sensitivity to light irradiation. This was observed in an experiment where Mo/Cu-OrpDg was irradiated during 3 h before addition of $[Ru(bpy)_3]^{2+}$. This pre-irradiation resulted into a less active enzyme (Figure S10). In a control experiment, pre-incubation of the protein during 3 h in the dark had only a very slight effect

on the activity (Figure S10). Note that ascorbate had no effect on the results whether it was added before or after the pre-irradiation step. The fact that the activity was much higher with no pre-irradiation indicates that Mo/Cu-OrpDg is protected from light-inactivation by the photosensitizer.

A previous report has shown that the ascorbate/$[Ru(bpy)_3]^{2+}$ system can be improved by addition of tris-(2-carboxyethyl)phosphine (TCEP), which serves to recycle oxidized ascorbate.[34] Figure S11 shows that this is also applicable here since a great increase of initial TOF (TOF° ~ 1200 h^{-1}) and TON after 4 h (TON ~ 2140) were obtained upon addition of TCEP.

Photocatalytic hydrogen evolution catalyzed by M/M'-OrpDg. Following the perspective opened by J. G. Moura regarding the possibility to assemble different dinuclear $[S_2MS_2M'S_2MS_2]^{3-}$ clusters within the binding pocket of OrpDg, we have prepared a series of *holo*-OrpDg proteins containing such clusters with M = Mo and M' = Cu, Fe, Ni, Co, Zn, Cd as well as with M = W and M' = Cu. The characteristic UV-visible spectra are shown in Figure S3 and are identical to those previously reported.[30] Following the optimized assay conditions developed above, we have evaluated their catalytic activity during photoreduction of protons and the results are given in Figure S12 & S13, showing clear differences between the different artificial enzymes. In Figure 6, the data are summarized in terms of TON at 2.5 hours and the initial rate (TOF°) value. The results show that the most active combination is the one with M = Mo and M' = Fe, followed by those with M = Mo and M' = Cu, Ni and Co. As shown in Figure 6, Mo/Fe-OrpDg achieves a remarkable TON of ~1150 after 2.5 hours of reaction. Orps carrying clusters with M' = Zn or Cd and M = Mo as well as with M' = Cu and M = W are much less active than Mo/Cu- and Mo/Fe-OrpDg. Mo/Ni-OrpDg displays very good TOF° (~ 680 h^{-1}), however, it seems to be less stable than Mo/Co- and Mo/Fe-OrpDg as shown by the much lower production of H_2 after 2.5 hours reaction ($TON_{2.5h}$ ~ 650). Finally, Mo/Cu-OrpTm proved as active as Mo/Cu-OrpDg (Figure S14).

Table S3 displays the maximum quantum yield for the various M/M'-OrpDg samples (see estimation details in the SI). The highest value, 0.29 %, was obtained for Mo/Fe-OrpDg. While very few artificial hydrogenase systems have been evaluated for their quantum efficiency, the value obtained here compares reasonably with a previous study reporting a quantum efficiency of 1 % using a ferredoxin-based Ru-Co hybrid system.[35]

Cyclic voltammetry experiments carried out under anaerobic conditions using a variety of M/M'-OrpDg preparations immobilized on pyrolytic graphite electrodes showed a large

catalytic wave at pH 5, corresponding to H_2 evolution reaction, with currents depending on the nature of the cluster (Figure S15). We could not detect non-turnover signals resulting from the stoichiometric reduction and oxidation of the protein, but these are often too faint. Control experiments with unmodified electrodes showed no redox activity indicating that the catalytic process was due to the protein at the surface of the electrode. The catalytic onset potential was in the range of -0.9 to -1.0 V vs NHE, consistent with the mechanism involving $[Ru(bpy)_3]^+$ (E= -1.23 V vs SHE) as the electron donor in the photosystem (see below).[36]

Computational Investigation of Hydrogen Evolution Reaction (HER) Mechanism. To better understand the photocatalytic HER properties of the Mo/Cu-OrpDg, we next investigated the reaction mechanism by performing Density Functional Theory (DFT) calculations. For the sake of computational efficiency, this mechanistic exploration was conducted using a model system that consists of a $[S_2MoS_2CuS_2MoS_2]^{3-}$ cluster, which was polarized by an implicit solvent model with a dielectric constant (ε) of 20 to account for the dielectric environment of the cluster at the protein-solvent interface[37] (see Computational Details section in the SI). Still, some key steps of the reaction mechanism were further analyzed by means of a larger cluster model obtained from a snapshot of the MD simulations (vide supra). This comprises, aside from the $[S_2MoS_2CuS_2MoS_2]^{3-}$ cluster, the OrpDg residues that were predicted to interact with the cluster in the *holo* form of the protein, including two positively charged amino acids (arginine and lysine), a polar tyrosine and other regions of the protein main chain that can establish hydrogen bonds with the cluster (see Figure S16).

Figure 7 shows the proposed catalytic cycle, which consists of three main steps, namely, the first and the second single electron transfer (1^{st} and 2^{nd} SET in Figure 7) of the $[S_2MoS_2CuS_2MoS_2]^{3-}$ cluster, and the H_2 formation step. The reaction begins with the photoexcitation of the $[Ru(bpy)_3]^{2+}$ photosensitizer by a visible light photon that leads to the triplet MLCT state, labeled as $[Ru(bpy)_3]^{2+,*}$.[38] This can be reductively quenched in a spontaneous manner (ΔG = -7.6 kcal mol^{-1}) by ascorbate ($HAsc^-$) to generate $[Ru(bpy)_3]^+$, which is a stronger reducing agent than $[Ru(bpy)_3]^{2+,*}$,[39] and an oxidized ascorbyl radical ($HAsc^{\bullet}$). The first SET from $[Ru(bpy)_3]^+$ to the $[S_2MoS_2CuS_2MoS_2]^{3-}$ cluster was predicted to be endergonic by 16.8 kcal mol^{-1} and to occur through a moderate free-energy barrier of 20.6 kcal mol^{-1}, which was estimated by means of the Marcus theory (see Computational Details section). Nonetheless, this process is rather sensitive to the chemical environment of the cluster. Specifically, when the cluster is embedded into the protein pocket, the energy of its LUMO, which is the molecular orbital accepting the extra electron, is lowered by ca. 0.8 eV

due to the stabilization of the polyanionic structure granted by the formation of hydrogen bonds with polar and positively charged residues of the protein. As a consequence, the SET from $[Ru(bpy)_3]^+$ to the cluster becomes much more favorable, being exergonic by 12.7 kcal mol^{-1} and exhibiting a significantly lower free-energy barrier of 4.8 kcal mol^{-1} (see values in parentheses in Figure 7). The extra electron in the one-electron reduced cluster is accommodated in one of the Mo centers, forming a Mo(V) species. Upon reduction, the terminal sulfide groups bound to the Mo(V) ion become more basic due to the increase of charge density and the $\pi^*_{Mo=S}$ nature of the populated molecular orbital, triggering the spontaneous association of a proton to a terminal sulfido group at neutral pH (see estimated pK_a values in Figure 7 and stability comparison with other isomers in Figure S17). Remarkably, the protonation of the cluster prevents undesired back electron transfer events from the reduced catalyst to the oxidized electron donor. It should be pointed out that although the $[S_2MoS_2CuS_2MoS_2]^{3-}$ cluster can be photoexcited under visible light irradiation, the resulting excited states are not expected to be involved in the reaction mechanism as no H_2 is experimentally observed in the absence of $[Ru(bpy)_3]^{2+}$ (*vide supra*).

Then, the $[H\{Mo^{V}Cu^{I}Mo^{VI}\}]^{3-}$ species can be further reduced by $[Ru(bpy)_3]^+$ through a second SET step, the free-energy barrier of which is estimated to be similar to that of the first SET (see Figure 7). This yields a mixed-valent Mo(IV)/Mo(VI) intermediate where both extra electrons are localized on the same Mo center in a triplet ground state configuration, albeit the most stable singlet state is only 5.6 kcal mol^{-1} higher in energy. This is caused by the effect that protonating a terminal sulfido group has on the electronic structure of the cluster, which stabilizes unoccupied molecular orbitals centered on the Mo(V) ion below those centered on the Mo(VI) (see Figures S18 and S19) The protonation of the resulting $[H\{Mo^{IV}Cu^{I}Mo^{VI}\}]^{4-}$ species is more favorable than that of the one-electron reduced species and, therefore, expected to occur spontaneously at the experimental pH. Again, the doubly protonated species is stabilized as a triplet, the lowest singlet being 0.6 (or 6.3 within the protein pocket) kcal mol^{-1} higher in energy (see Figure 7).

The $[H_2\{Mo^{IV}Cu^{I}Mo^{VI}\}]^{3-}$ species was found to be able to evolve H_2 through a stepwise process that begins with thermally-activated internal conversion from the triplet ground state ($^3H_2[\{Mo^{IV}Cu^{I}Mo^{VI}\}]^{3-}$ to the lowest singlet excited state ($^1H_2\{Mo^{IV}Cu^{I}Mo^{VI}\}]^{3-}$), in which one of the terminal H atoms supports a slightly higher electron density than the other, as suggested by the analysis of atomic charges (see Table S6). This is followed by the attack of a terminal sulfur hydride to the proton of the neighboring thiol group in the singlet state, which occurs through ^{1}**TS$_{HER}$** (see Figure 7 and Figure S20 for a 3D representation of the optimized

geometry) and readily releases H_2, regenerating the fully oxidized form of the cluster and closing the catalytic cycle. The latter process requires overcoming a very low free-energy barrier of 4.3 kcal mol^{-1} from $^1[H_2\{Mo^{IV}Cu^{I}Mo^{VI}\}]^{3-}$, which accounts for an overall free-energy barrier of 4.9 kcal mol^{-1} from the triplet ground state configuration. Note that the H_2 formation step is significantly less sensitive to the environment compared to SET and protonation processes, although we observed an increase of the overall free-energy barrier from 4.9 to a still very smooth barrier of 10.5 kcal mol^{-1} upon embedding the cluster into the protein pocket. This mainly arises from the stabilization of the triplet ground state with respect to the reactive singlet state, which is more pronounced within the protein scaffold (Figure 7).

Similar HER mechanisms where a metallothiol plays the role of hydride donor have been proposed for both Mo-based molecular[40] and heterogeneous catalysts,[41-43] on the basis of DFT and experimental spectroscopic analyses. Still, alternative HER mechanisms whereby a Mo-hydride is formed from the $[H_2\{Mo^{IV}Cu^{I}Mo^{VI}\}]^{3-}$ species were also explored, although they were found to be much higher in energy (see Figure S21). It is worth mentioning that a Mo(III)-hydride has been recently proposed as a key intermediate in the electrocatalytic HER by amorphous MoS_x.[44] However, it is rather unlikely that such a low redox state is formed in the Mo/Cu-OrpDg system, considering that the doubly-reduced cluster can already attain the formation of H_2 through a free-energy barrier that can be readily overcome at room temperature.

Finally, we sought to rationalize the observed lack of CO_2RR activity of the Mo/Cu-OrpDg enzyme. On the basis of the hydride-transfer reactivity responsible for the HER, we evaluated the feasibility of a hydride transfer from $[H_2(Mo^{IV}Cu^{I}Mo^{VI}\}]^{3-}$ to an incoming CO_2 molecule to generate formate (see Figure S22 for a representation of the transition state structure). In agreement with the experimental results, this process was found to entail a free-energy barrier of 16.7 kcal mol^{-1}, significantly higher than that governing the H_2 formation (4.9 kcal mol^{-1}), thus rendering the CO_2RR pathway unable to compete with the much faster HER pathway.

Finally, we performed additional DFT calculations seeking to rationalize the experimental reactivity trends observed along the M/M'-OrpDg series. To this end, we characterized the whole HER mechanism for a set of representative, experimentally-tested clusters ($[\{MoFeMo\}]^{3-}$, $[\{WCuW\}]^{3-}$ and $[\{MoCdMo\}]^{2-}$) and compared their thermodynamic and kinetic features with those of $[\{MoCuMo\}]^{3-}$ in Table S7.

In agreement with the experimental results, $[\{WCuW\}]^{3-}$ is significantly more difficult to reduce compared to $[\{MoCuMo\}]^{3-}$ and therefore, less active for HER. This can be explained by the higher energy of unoccupied molecular orbitals of the W-based compound (E_{LUMO} = -1.48 vs -1.83 eV for $[\{WCuW\}]^{3-}$ and $[\{MoCuMo\}]^{3-}$, respectively). In fact, the higher electron affinity of Mo(VI)- compared to W(VI)-based analogues is a well-known feature in other fields, such as in polyoxometalate chemistry.[45] On the opposite end, the $[\{MoCdMo\}]^{2-}$, bearing a less negative overall charge, can be more easily reduced (see Table S7). However, this cluster also exhibits a significantly lower basicity (see Tables S7 and S8), which decreases the ability of the reduced complex to bind protons, being thus detrimental to catalysis. Finally, in line with the similar reaction rates observed experimentally for $[\{MoFeMo\}]^{3-}$ and $[\{MoCuMo\}]^{3-}$, these were found to exhibit very similar barriers both for SET and H_2 formation steps, lying within the limits of computational uncertainty, along with a basicity that enables their protonation under experimental conditions (see Table S7). Further details on the electronic structures of M/M' clusters and their calculated reaction mechanisms can be found in the SI (Figures S23 - S26).

Conclusions.

While artificial enzymology has emerged as a very attractive approach to understand key aspects of catalysis and to find out new classes of catalysts for a variety of reactions, artificial hydrogenases, having the potential to catalyze light-driven proton reduction into hydrogen, are more recent. In Table S9, we provide the list of previously studied artificial systems which proved catalytically active during light-induced HER (hydrogen evolution reaction). Surprisingly, the previously reported examples are, almost exclusively, based on dinuclear iron complexes, mimicking one class of natural hydrogenases, and cobalt CoNx complexes (Co-porphyrins, cobaloximes and Co-triazacyclononane). The very few exceptions are proteins engineered for binding one Ni ion. Here we have described our discovery of a new class of HER catalysts, namely a trimetallic cluster, $[S_2MoS_2MS_2MoS_2]^{3-}$, with M = Fe, Cu, Co, Ni, which, upon binding to the Orange Protein (Orp), a protein of unknown function, converts it into an active hydrogenase. To our knowledge, the MoFeMo version (Mo/Fe-OrpDg) is by far the most active artificial hydrogenase reported so far, with an initial turnover frequency of 890 h^{-1} and reaching a TON of 1150 after 2.5 hours reaction (Table S9). DFT calculations have not only confirmed that photocatalytic HER by such clusters within the protein is feasible but also established a possible reaction mechanism, in which the MoS_4 moiety is the catalytic redox site and the sulfur ligands function as proton-binding sites

(Figure 7). They also show that the nature of both central and peripheral metal ions is critical for tuning the electronic structure of the cluster, explaining the differences between the various clusters in terms of catalytic activity, which is determined by the delicate balance between the ability of the cluster to accept electrons and that of its reduced form to associate protons and activate them. The detailed characterization of the Mo/Cu-OrpDg version, by a variety of spectroscopies, structure modeling with *in silico* docking and molecular dynamics, following a previous NMR characterization,[28] led us, in the absence of X-ray three-dimensional structure of the *holo*-protein, to get a clear knowledge of the cluster binding site and of the amino acid residues interacting with the cluster. This information provides a strong basis for further studies of the reaction mechanism aiming at tuning the reactivity of this fascinating system.

ASSOCIATED CONTENT. Additional experimental details: materials and reagents; cloning, expression, reconstitution and purification of proteins; light absorption and X-ray absorption spectroscopy; molecular docking and molecular dynamics; photocatalytic experiments; DFT calculations and Supporting Information.

Notes. The authors declare no competing financial interest.

ACKNOWLEDGMENTS. R.L. acknowledges financial support from Sorbonne Université. M.A. is grateful to the CEA for permitting his stay at the Collège de France for two years as invited researcher. We are grateful to Ludovic Pecqueur for initial structural models of *holo*-ORP. The project has received funding from CNRS, CEA, Sorbonne Université and Collège de France. We acknowledge the European Synchrotron Radiation Facility for provision of synchrotron radiation facilities and we would like to thank Olivier Proux for assistance in using beamline BM30.

We acknowledge funding from :

Agence Nationale de la Recherche (Labex ARCANE, CBH-EUR-GS, ANR-17-EURE-0003) (M.A., G.V., P.C. and R.B.).

The French State Program ‘Investissements d’Avenir’ (Grants “LABEX DYNAMO”, ANR-11-LABX-0011 (M.F., Y. L., R. J. L. and B.F.).

References.

1. Armstrong, F. A.; Belsey, N. A.; Cracknell, J. A.; Goldet, G.; Parkin, A.; Reisner, E.; Vincent, K. A.; Wait, A. F., Dynamic electrochemical investigations of hydrogen oxidation and production by enzymes and implications for future technology. *Chemical Society Reviews* **2009,** *38* (1), 36-51.
2. Lubitz, W.; Ogata, H.; Rudiger, O.; Reijerse, E., Hydrogenases. *Chem Rev* **2014,** *114* (8), 4081-4148.
3. Stripp, S. T.; Duffus, B. R.; Fourmond, V.; Leger, C.; Leimkuhler, S.; Hirota, S.; Hu, Y.; Jasniewski, A.; Ogata, H.; Ribbe, M. W., Second and Outer Coordination Sphere Effects in Nitrogenase, Hydrogenase, Formate Dehydrogenase, and CO Dehydrogenase. *Chem Rev* **2022,** *122* (14), 11900-11973.
4. Appel, A. M.; Bercaw, J. E.; Bocarsly, A. B.; Dobbek, H.; DuBois, D. L.; Dupuis, M.; Ferry, J. G.; Fujita, E.; Hille, R.; Kenis, P. J. A.; Kerfeld, C. A.; Morris, R. H.; Peden, C. H. F.; Portis, A. R.; Ragsdale, S. W.; Rauchfuss, T. B.; Reek, J. N. H.; Seefeldt, L. C.; Thauer, R. K.; Waldrop, G. L., Frontiers, Opportunities, and Challenges in Biochemical and Chemical Catalysis of CO2 Fixation. *Chem Rev* **2013,** *113* (8), 6621-6658.
5. Wittenborn, E. C.; Guendon, C.; Merrouch, M.; Benvenuti, M.; Fourmond, V.; Leger, C.; Drennan, C. L.; Dementin, S., The Solvent-Exposed Fe-S D-Cluster Contributes to Oxygen-Resistance in Desulfovibrio vulgaris Ni-Fe Carbon Monoxide Dehydrogenase. *Acs Catal* **2020,** *10* (13), 7328-7335.
6. Chaudhary, Y. S.; Woolerton, T. W.; Allen, C. S.; Warner, J. H.; Pierce, E.; Ragsdale, S. W.; Armstrong, F. A., Visible light-driven CO2 reduction by enzyme coupled CdS nanocrystals. *Chem Commun* **2012,** *48* (1), 58-60.
7. Robinson, W. E.; Bassegoda, A.; Blaza, J. N.; Reisner, E.; Hirst, J., Understanding How the Rate of C-H Bond Cleavage Affects Formate Oxidation Catalysis by a Mo-Dependent Formate Dehydrogenase. *J Am Chem Soc* **2020,** *142* (28), 12226-12236.
8. Wang, V. C. C.; Ragsdale, S. W.; Armstrong, F. A., Investigations of the Efficient Electrocatalytic Interconversions of Carbon Dioxide and Carbon Monoxide by Nickel-Containing Carbon Monoxide Dehydrogenases. *Metal Ions Life Sci* **2014,** *14*, 71-97.
9. Calzadiaz-Ramirez, L.; Meyer, A. S., Formate dehydrogenases for CO (2) utilization. *Curr Opin Biotech* **2022,** *73*, 95-100.
10. Contaldo, U.; Curtil, M.; Perard, J.; Cavazza, C.; Le Goff, A., A Pyrene-Triazacyclononane Anchor Affords High Operational Stability for CO2RR by a CNT-Supported Histidine-Tagged CODH. *Angew Chem Int Edit* **2022,** *61* (21).
11. Meneghello, M.; Leger, C.; Fourmond, V., Electrochemical Studies of CO(2) -Reducing Metalloenzymes. *Chemistry* **2021,** *27* (70), 17542-17553.
12. Meneghello, M.; Uzel, A.; Broc, M.; Manuel, R. R.; Magalon, A.; Leger, C.; Pereira, I. A. C.; Walburger, A.; Fourmond, V., Electrochemical Kinetics Support a Second Coordination Sphere Mechanism in Metal-Based Formate Dehydrogenase. *Angew Chem Int Ed Engl* **2023,** *62* (6), e202212224.
13. Schwizer, F.; Okamoto, Y.; Heinisch, T.; Gu, Y. F.; Pellizzoni, M. M.; Lebrun, V.; Reuter, R.; Kohler, V.; Lewis, J. C.; Ward, T. R., Artificial Metalloenzymes: Reaction Scope and Optimization Strategies. *Chem Rev* **2018,** *118* (1), 142-231.
14. Caserta, G.; Roy, S.; Atta, M.; Artero, V.; Fontecave, M., Artificial hydrogenases: biohybrid and supramolecular systems for catalytic hydrogen production or uptake. *Current Opinion in Chemical Biology* **2015,** *25*, 36-47.
15. Le, J. M.; Bren, K. L., Engineered Enzymes and Bioinspired Catalysts for Energy Conversion. *Acs Energy Lett* **2019,** *4* (9), 2168-2180.
16. Prasad, P.; Selvan, D.; Chakraborty, S., Biosynthetic Approaches towards the Design of Artificial Hydrogen-Evolution Catalysts. *Chem-Eur J* **2020,** *26* (55), 12494-12509.
17. DiPrimio, D. J.; Holland, P. L., Repurposing metalloproteins as mimics of natural metalloenzymes for small-molecule activation. *Journal of Inorganic Biochemistry* **2021,** *219*.
18. Yokoi, N.; Miura, Y.; Huang, C. Y.; Takatani, N.; Inaba, H.; Koshiyama, T.; Kanamaru, S.; Arisaka, F.; Watanabe, Y.; Kitagawa, S.; Ueno, T., Dual modification of a triple-stranded beta-helix

nanotube with Ru and Re metal complexes to promote photocatalytic reduction of CO2. *Chem Commun* **2011,** *47* (7), 2074-2076.
19. Schneider, C. R.; Shafaat, H. S., An internal electron reservoir enhances catalytic CO2 reduction by a semisynthetic enzyme. *Chem Commun* **2016,** *52* (64), 9889-9892.
20. Schneider, C. R.; Manesis, A. C.; Stevenson, M. J.; Shafaat, H. S., A photoactive semisynthetic metalloenzyme exhibits complete selectivity for CO2 reduction in water. *Chem Commun* **2018,** *54* (37), 4681-4684.
21. Liu, X. H.; Kang, F. Y.; Hu, C.; Wang, L.; Xu, Z.; Zheng, D. D.; Gong, W. M.; Lu, Y.; Ma, Y. H.; Wang, J. Y., A genetically encoded photosensitizer protein facilitates the rational design of a miniature photocatalytic CO2-reducing enzyme. *Nature Chemistry* **2018,** *10* (12), 1201-1206.
22. Kang, F. Y.; Yu, L.; Xia, Y.; Yu, M. L.; Xia, L.; Wang, Y. C. A.; Yang, L.; Wang, T. Y.; Gong, W. M.; Tian, C. L.; Liu, X. H.; Wang, J. Y., Rational Design of a Miniature Photocatalytic CO2-Reducing Enzyme. *Acs Catal* **2021,** *11* (9), 5628-5635.
23. Bursakov, S. A.; Gavel, O. Y.; Di Rocco, G.; Lampreia, J.; Calvete, J.; Pereira, A. S.; Moura, J. J. G.; Moura, I., Antagonists Mo and Cu in a heterometallic cluster present on a novel protein (orange protein) isolated from Desulfovibrio gigas. *Journal of Inorganic Biochemistry* **2004,** *98* (5), 833-840.
24. Dobbek, H.; Gremer, L.; Kiefersauer, R.; Huber, R.; Meyer, O., Catalysis at a dinuclear [CuSMo(==O)OH] cluster in a CO dehydrogenase resolved at 1.1-angstrom resolution. *P Natl Acad Sci USA* **2002,** *99* (25), 15971-15976.
25. George, G. N.; Pickering, I. J.; Yu, E. Y.; Prince, R. C.; Bursakov, S. A.; Gavel, O. Y.; Moura, I.; Moura, J. J. G., A novel protein-bound copper - Molybdenum cluster. *J Am Chem Soc* **2000,** *122* (34), 8321-8322.
26. Maiti, B. K.; Pal, K.; Sarkar, S., A structural model of mixed metal sulfide cluster of molybdenum and copper present in the orange protein of Desulfovibrio gigas. *Inorg Chem Commun* **2004,** *7* (9), 1027-1029.
27. Najmudin, S.; Bonifacio, C.; Duarte, A. G.; Pualeta, S. R.; Moura, I.; Moura, J. J. G.; Romao, M. J., Crystallization and crystallographic analysis of the apo form of the orange protein (ORP) from Desulfovibrio gigas. *Acta Crystallographica Section F-Structural Biology Communications* **2009,** *65*, 730-732.
28. Carepo, M. S. P.; Pauleta, S. R.; Wedd, A. G.; Moura, J. J. G.; Moura, I., Mo-Cu metal cluster formation and binding in an orange protein isolated from Desulfovibrio gigas. *Journal of Biological Inorganic Chemistry* **2014,** *19* (4-5), 605-614.
29. Carepo, M. S. P.; Carreira, C.; Grazina, R.; Zakrzewska, M. E.; Dolla, A.; Aubert, C.; Pauleta, S. R.; Moura, J. J. G.; Moura, I., Orange protein from Desulfovibrio alaskensis G20: insights into the Mo-Cu cluster protein-assisted synthesis. *Journal of Biological Inorganic Chemistry* **2016,** *21* (1), 53-62.
30. Maiti, B. K.; Maia, L. B.; Paueta, S. R.; Moura, I.; Moura, J. J. G., Protein-Assisted Formation of Molybdenum Heterometallic Clusters: Evidence for the Formation of S2MoS2-M-S2MoS2 Clusters with M = Fe, Co, Ni, Cu, or Cd within the Orange Protein. *Inorg Chem* **2017,** *56* (4), 2210-2220.
31. Pickering, I. J.; George, G. N.; Dameron, C. T.; Kurz, B.; Winge, D. R.; Dance, I. G., X-Ray-Absorption Spectroscopy of Cuprous Thiolate Clusters in Proteins and Model Systems. *J Am Chem Soc* **1993,** *115* (21), 9498-9505.
32. Jullien, A. S.; Gateau, C.; Kieffer, I.; Testemale, D.; Delangle, P., X-ray Absorption Spectroscopy Proves the Trigonal-Planar Sulfur-Only Coordination of Copper(I) with High-Affinity Tripodal Pseudopeptides. *Inorg Chem* **2013,** *52* (17), 9954-9961.
33. Thomsen, R.; Christensen, M. H., MolDock: A new technique for high-accuracy molecular docking. *Journal of Medicinal Chemistry* **2006,** *49* (11), 3315-3321.
34. Bachmann, C.; Probst, B.; Guttentag, M.; Alberto, R., Ascorbate as an electron relay between an irreversible electron donor and Ru(II) or Re(I) photosensitizers. *Chem Commun (Camb)* **2014,** *50* (51), 6737-9.
35. Soltau, S. R.; Dahlberg, P. D.; Niklas, J.; Poluektov, O. G.; Mulfort, K. L.; Utschig, L. M., Ru-protein-Co biohybrids designed for solar hydrogen production: understanding electron transfer pathways related to photocatalytic function. *Chemical Science* **2016,** *7* (12), 7068-7078.

36. Lehn, J. M.; Ziessel, R., Photochemical Reduction of Carbon-Dioxide to Formate Catalyzed by 2,2'-Bipyridine-Ruthenium(Ii) or 1,10-Phenanthroline-Ruthenium(Ii) Complexes. *J Organomet Chem* **1990,** *382* (1-2), 157-173.
37. Li, L.; Li, C.; Zhang, Z.; Alexov, E., On the 'Dielectric "Constant" of Proteins: Smooth Dielectric Function for Macromolecular Modeling and Its Implementation in DelPhi. *Journal of Chemical Theory and Computation* **2013,** *9* (4), 2126-2136.
38. Durham, B.; Caspar, J. V.; Nagle, J. K.; Meyer, T. J., Photochemistry of Ru(Bpy)32+. *J Am Chem Soc* **1982,** *104* (18), 4803-4810.
39. Prier, C. K.; Rankic, D. A.; MacMillan, D. W. C., Visible Light Photoredox Catalysis with Transition Metal Complexes: Applications in Organic Synthesis. *Chem Rev* **2013,** *113* (7), 5322-5363.
40. Yang, T. L.; Ni, S. F.; Qin, P.; Dang, L., A mechanism study on the hydrogen evolution reaction catalyzed by molybdenum disulfide complexes. *Chem Commun* **2018,** *54* (9), 1113-1116.
41. Deng, Y. L.; Ting, L. R. L.; Neo, P. H. L.; Zhang, Y. J.; Peterson, A. A.; Yeo, B. S., Operando Raman Spectroscopy of Amorphous Molybdenum Sulfide (MoSx) during the Electrochemical Hydrogen Evolution Reaction: Identification of Sulfur Atoms as Catalytically Active Sites for H+ Reduction. *Acs Catal* **2016,** *6* (11), 7790-7798.
42. Ting, L. R. L.; Deng, Y. L.; Ma, L.; Zhang, Y. J.; Peterson, A. A.; Yeo, B. S., Catalytic Activities of Sulfur Atoms in Amorphous Molybdenum Sulfide for the Electrochemical Hydrogen Evolution Reaction. *Acs Catal* **2016,** *6* (2), 861-867.
43. Lassalle-Kaiser, B.; Merki, D.; Vrubel, H.; Gul, S.; Yachandra, V. K.; Hu, X. L.; Yano, J., Evidence from in Situ X-ray Absorption Spectroscopy for the Involvement of Terminal Disulfide in the Reduction of Protons by an Amorphous Molybdenum Sulfide Electrocatalyst. *J Am Chem Soc* **2015,** *137* (1), 314-321.
44. Bau, J. A.; Emwas, A. H.; Nikolaienko, P.; Aljarb, A. A.; Tung, V.; Rueping, M., Mo3+ hydride as the common origin of H-2 evolution and selective NADH regeneration in molybdenum sulfide electrocatalysts. *Nat Catal* **2022,** *5* (5), 397-404.
45. Gumerova, N. I.; Rompel, A., Synthesis, structures and applications of electron-rich polyoxometalates. *Nat Rev Chem* **2018,** *2* (2).

Figures and legends.

Scheme 1.

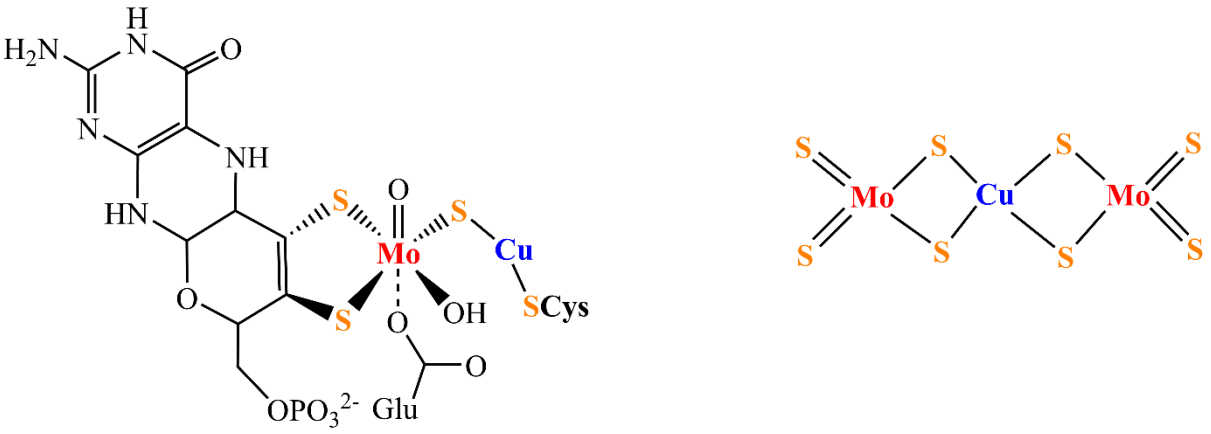

Scheme 1: Left: structure of Mo-Cu active site of carbon monoxide dehydrogenase. Right: structure of the $[S_2MoS_2CuS_2MoS_2]^{3-}$ cluster of OrpDg. Mo is in red, Cu in blue and sulfur in orange.

Figure 1.

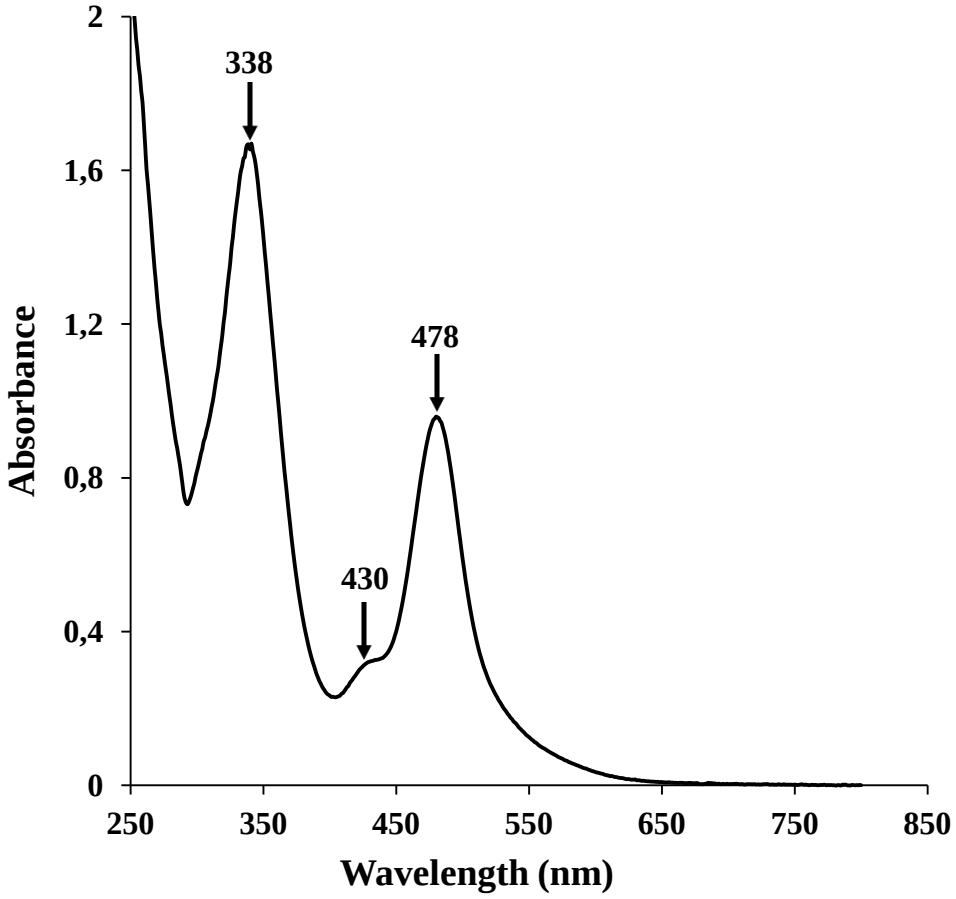

Figure 1: UV–visible spectrum of the Mo/Cu-OrpDg. The spectrum was recorded with 117 µM of Mo/Cu-OrpDg in 50 mM Tris-Cl pH 7.5. The arrows indicate the 338-nm, 430-nm and 478-nm S→Mo charge-transfer bands.

Figure 2.

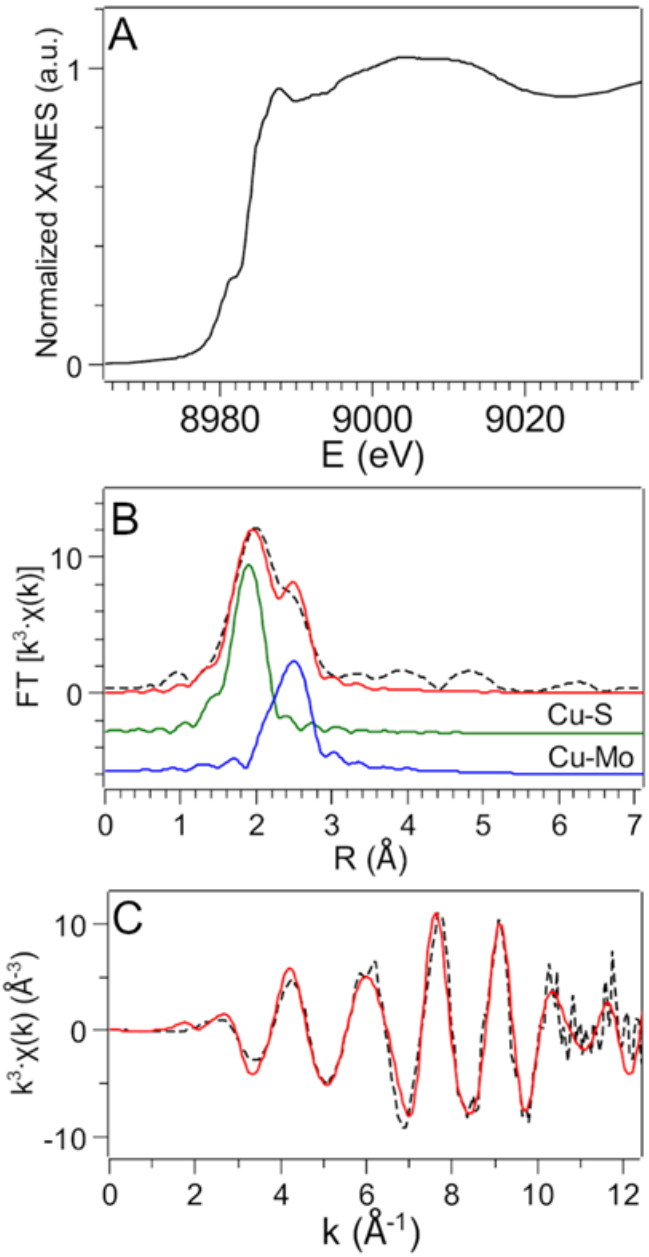

Figure 2: Cu K-edge X-ray absorption spectra of Mo/Cu-OrpDg. (A) Experimental X-ray absorption near edge structure (XANES) spectrum. (B) Fourier-Transformed EXAFS spectra: experimental (black, dashed curve) and simulated signal (red, solid line) based on a two-shell model including the single scattering contributions from Cu-S and Cu-Mo (green and blue line, respectively, shifted for clarity). (C) Experimental (black, dashed) k^3-weighted EXAFS spectrum and best-fitting theoretical curve (red, solid) generated *ab initio* based on a $[S_2MoS_2CuS_2MoS_2]^{3-}$ cluster model.

Figure 3.

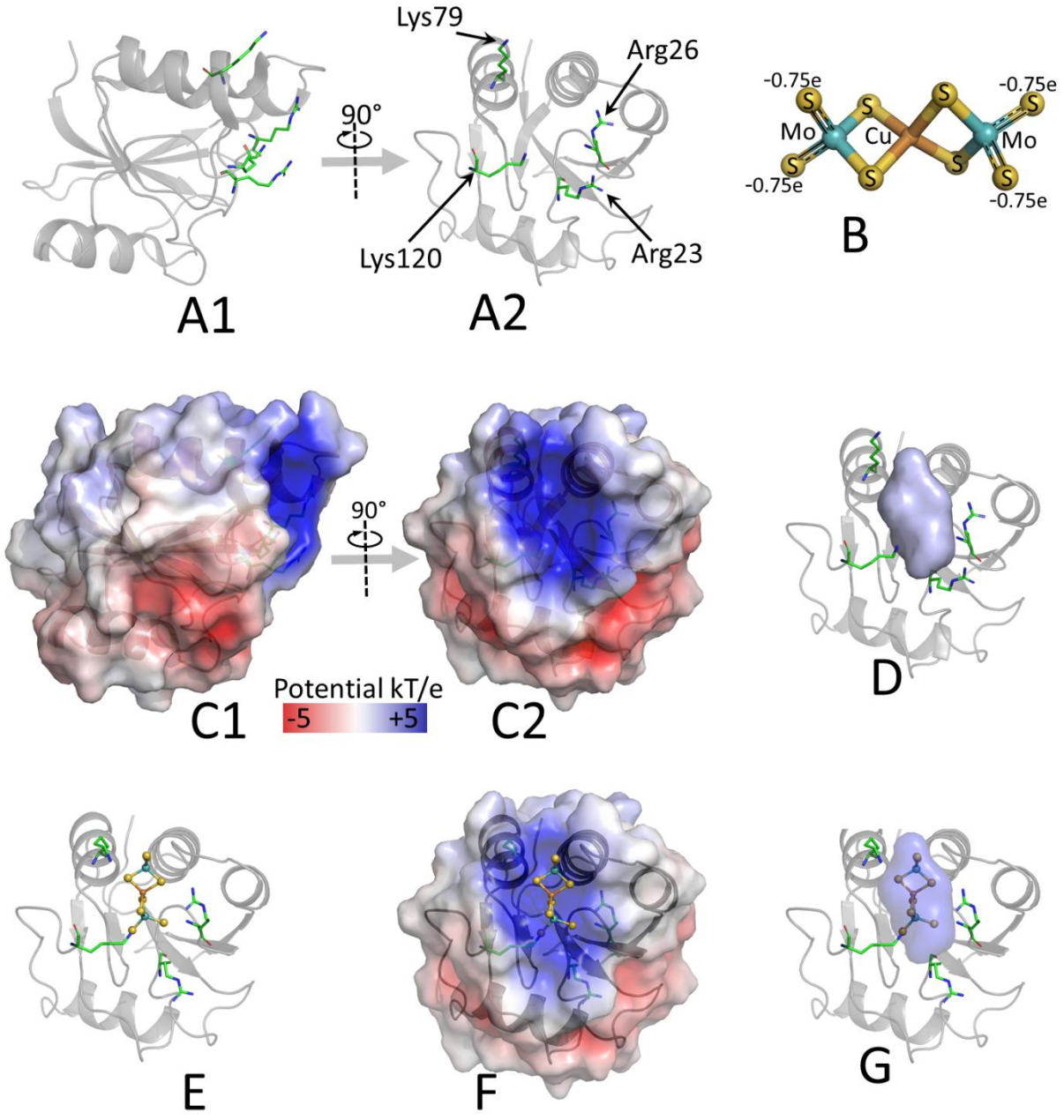

Figure 3: Docking simulation of the metal complex $[S_2MoS_2CuS_2MoS_2]^{3-}$ in the *apo*-OrpDg using Molegro Virtual Docker (MVD). **A1 and A2:** Crystallographic structure of the *apo*-OrpDg drawn as cartoon representation. Side chains of Lys-79, Arg-23, Arg-26, Lys-79 and Lys-120, defined as flexible in MVD, are highlighted in stick representation. **B:** structure the metal-complex in stick representation. **C1 and C2**: Electrostatic potential surface of the *apo*-Orp, red and blue colors reveal the negatively and positively charged area respectively. **D:** Volume of the single pocket at the surface of the *apo*-OrpDg calculated by MVD**. E:** Structure of the best docking pose selected on the basis of MVD energy score**. F and G:** Best binding position of the metal-cluster at the protein surface fitting the positive electrostatic potential zone and the pocket volume.

Figure 4.

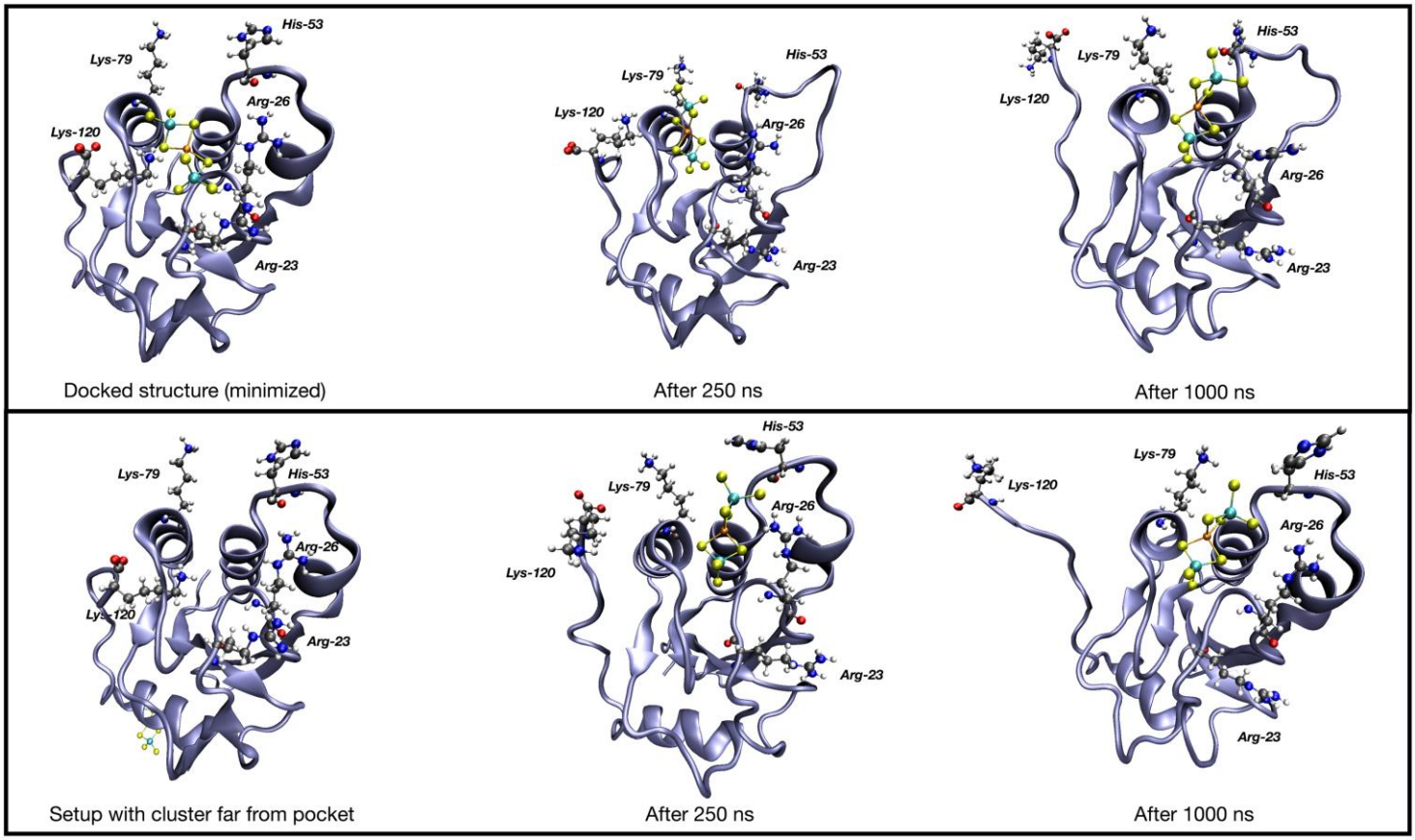

Figure 4: Snapshots taken from classical simulations, starting from docked (top) and non-docked (bottom) structures. Initial minimized structures shown (left), after 250 ns (middle) and after 1000 ns (right).

Figure 5.

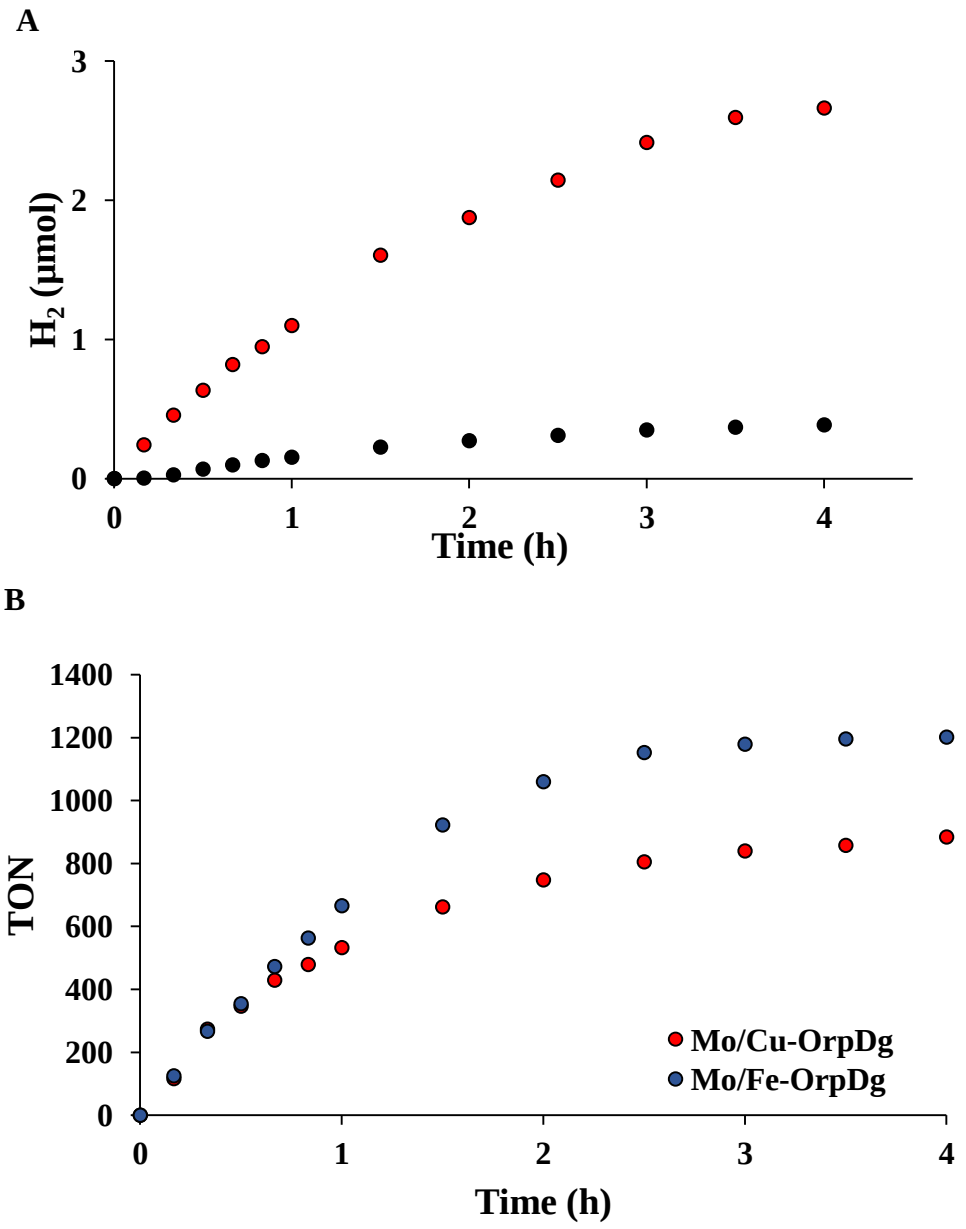

Figure 5. Photocatalytic activity for H_2 evolution by *holo*-OrpDg.
(A) Amount of H_2 produced in presence (red circles) and in absence (dark circles) of Mo/Cu-OrpDg. Conditions: photocatalysis was carried out in a 2 ml N_2-saturated solution containing 5 µM Mo/Cu-OrpDg, 100 µM $[Ru(bpy)_3]Cl_2$, 100 mM L-AscHNa, 100 mM potassium phosphate buffer (pH 6.8).
(B) Optimal conditions for H_2 evolution using Mo/Cu-OrpDg (red circles) and Mo/Fe-OrpDg (blue circles): TON (nmol of H_2 produced / nmol of catalyst). Conditions: photocatalysis was carried out in a 2 ml N_2-saturated solution containing 5 µM Mo/Cu-OrpDg or Mo/Fe-OrpDg, 700 µM $[Ru(bpy)_3]Cl_2$, 100 mM L-AscHNa, 100 mM sodium citrate buffer (pH 5.2), T = 20 °C, using Xe lamp irradiation (λ > 415 nm).

Figure 6.

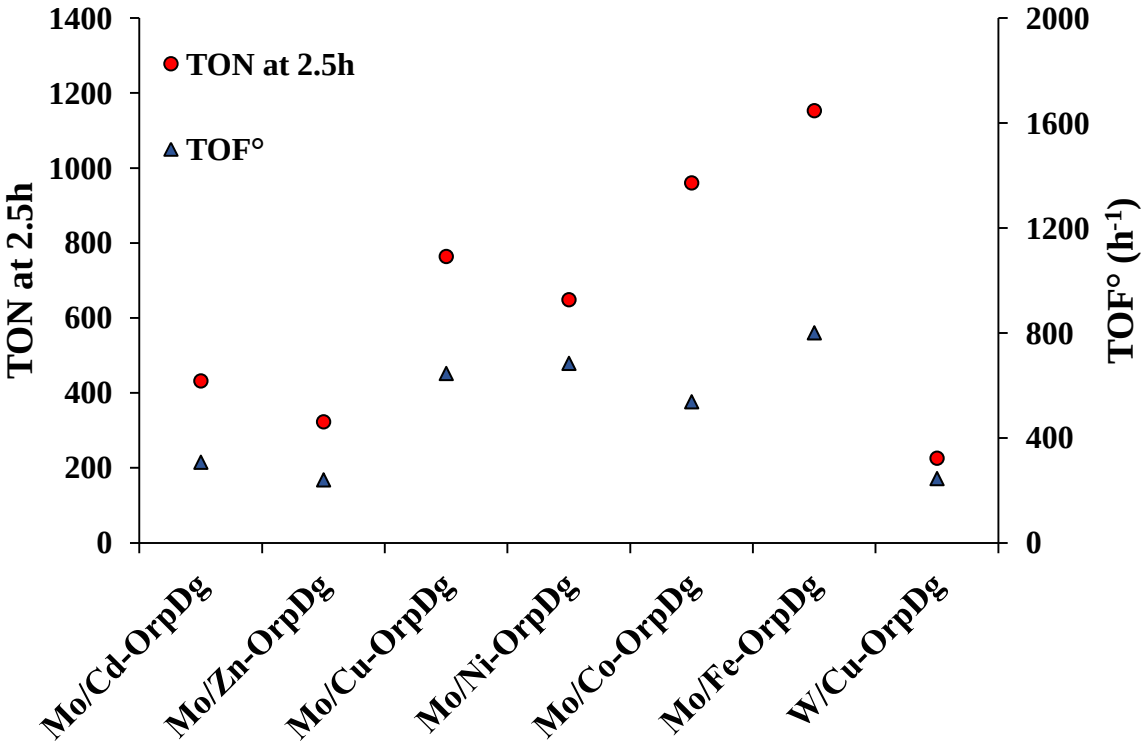

Figure 6. Plot of the activity for H_2 evolution versus the *holo*-Orp derivatives. Red dots: TON at 2.5 hours of irradiation; blue triangles: TOF°. Conditions: photocatalysis was carried out in a 2 ml N_2-saturated solution containing 5 µM *holo*-Orp derivatives, 700 µM $[Ru(bpy)_3]Cl_2$, 100 mM L-AscHNa, 100 mM sodium citrate buffer (pH 5.2), T = 20 °C, using Xe lamp irradiation (λ > 415 nm).

Figure 7.

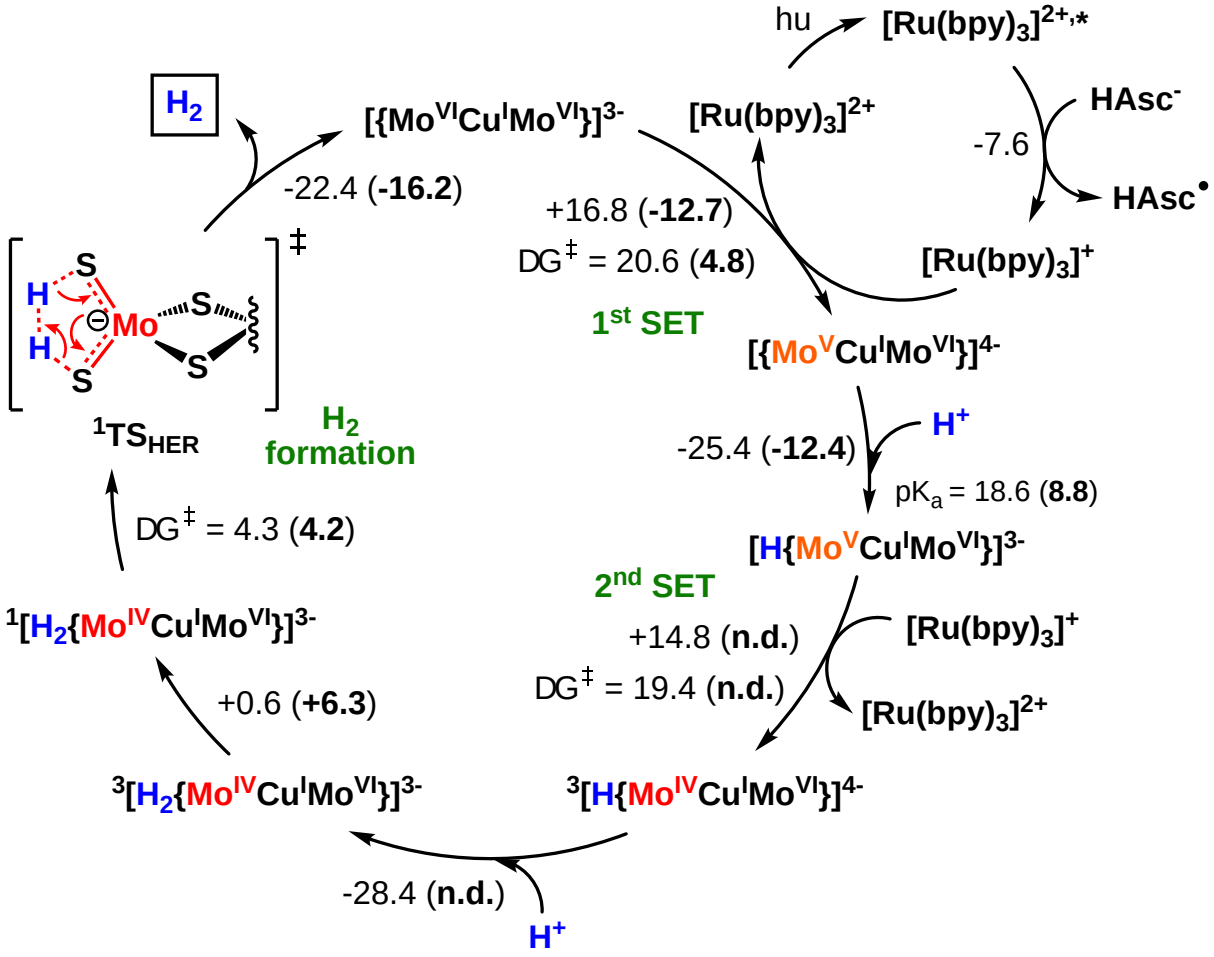

Figure 7. Proposed reaction mechanism for the photocatalytic HER promoted by the $[S_2MoS_2CuS_2MoS_2]^{3-}$ cluster of *holo*-OrpDg. Standard-state reaction Gibbs free energies and free-energy barriers are given in kcal mol^{-1}. Bolded values in parentheses were obtained from calculations on a larger cluster model system that explicitly incorporates the protein residues surrounding the $[S_2MoS_2CuS_2MoS_2]^{3-}$ cluster in the *holo*-ORPDg (see Computational Details and Figure S16 for a graphical representation of the models). The 'n.d.' notation stands for 'not determined', as only key steps of the mechanism were analyzed on a larger cluster model.

ToC graphic.

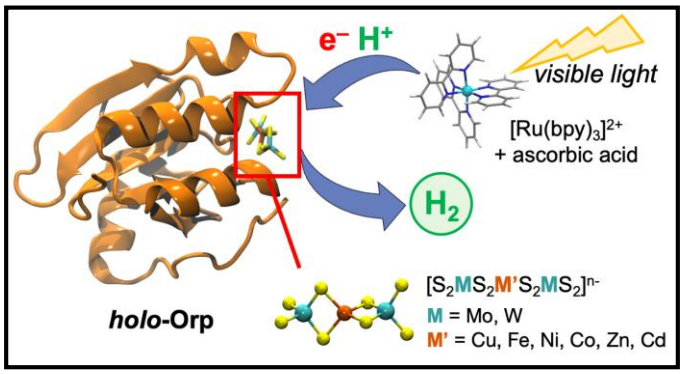
e⁻ H⁺
visible light
[Ru(bpy)3]2+
+ ascorbic acid
H2
holo-Orp
[S2MS2M'S2MS2]n-
M = Mo, W
M' = Cu, Fe, Ni, Co, Zn, Cd